Check for updates

Received: 1 August 2023 | Revised: 20 September 2023 | Accepted: 1 October 2023

DOI: 10.1002/cey2.487

RESEARCH ARTICLE

CARBON ENERGY WILEY

Stable immobilization of lithium polysulfides using three-dimensional ordered mesoporous Mn_2O_3 as the host material in lithium–sulfur batteries

Sung Joon Park[1] | **Yun Jeong Choi**[2] | **Hyun-seung Kim**[3] | **Min Joo Hong**[4] | **Hongjun Chang**[5] | **Janghyuk Moon**[5] | **Young-Jun Kim**[6,7] | **Junyoung Mun**[7,8] | **Ki Jae Kim**[1,7]

[1]Department of Energy Science, Sungkyunkwan University, Suwon, Gyeonggi-do, Republic of Korea

[2]Department of Energy Engineering, Konkuk University, Seoul, Republic of Korea

[3]Advanced Batteries Research Center, Korea Electronic Technology Institute, Seongnam, Republic of Korea

[4]Department of Future Energy Engineering, Sungkyunkwan University, Suwon, Republic of Korea

[5]Department of Energy Systems Engineering, Chung-Ang University, Seoul, Republic of Korea

[6]SKKU Advanced Institute of Nanotechnology, Sungkyunkwan University, Suwon, Gyeonggi-do, Republic of Korea

[7]SKKU Institute of Energy Science and Technology (SIEST), Sungkyunkwan University, Suwon, Republic of Korea

[8]School of Advanced Materials Science and Engineering, Sungkyunkwan University, Suwon, Republic of Korea

Correspondence

Young-Jun Kim, SKKU Advanced Institute of Nanotechnology, Sungkyunkwan University, 83212 Research Complex 2, 2066 Seobu-ro, Jangan-gu, Suwon 16419, Gyeonggi-do, Republic of Korea.
Email: yjkim68@skku.edu

Junyoung Mun, School of Advanced Materials Science and Engineering, Sungkyunkwan University, 16419 Suwon, Republic of Korea.
Email: munjy@skku.edu

Ki Jae Kim, SKKU Institute of Energy Science and Technology (SIEST), Sungkyunkwan University, 16419 Suwon, Republic of Korea.
Email: kijaekim@skku.edu

Funding information

Ministry of Trade, Industry and Energy, Grant/Award Number: 20010095; Korea Evaluation Institute of Industrial Technology, Grant/Award Number: 20012341

Abstract

Lithium–sulfur batteries (LSBs) have drawn significant attention owing to their high theoretical discharge capacity and energy density. However, the dissolution of long-chain polysulfides into the electrolyte during the charge and discharge process ("shuttle effect") results in fast capacity fading and inferior electrochemical performance. In this study, Mn_2O_3 with an ordered mesoporous structure (OM-Mn_2O_3) was designed as a cathode host for LSBs via KIT-6 hard templating, to effectively inhibit the polysulfide shuttle effect. OM-Mn_2O_3 offers numerous pores to confine sulfur and tightly anchor the dissolved polysulfides through the combined effects of strong polar–polar interactions, polysulfides, and sulfur chain catenation. The OM-Mn_2O_3/S composite electrode delivered a discharge capacity of 561 mA h g^{-1} after 250 cycles at 0.5 C owing to the excellent performance of OM-Mn_2O_3. Furthermore, it retained a discharge capacity of 628 mA h g^{-1} even at a rate of 2 C, which was significantly higher than that of a pristine sulfur electrode (206 mA h g^{-1}). These findings provide a prospective strategy for designing cathode materials for high-performance LSBs.

KEYWORDS

host material, lithium–sulfur battery, ordered mesoporous structure, shuttle effect, transition-metal oxides

This is an open access article under the terms of the Creative Commons Attribution License, which permits use, distribution and reproduction in any medium, provided the original work is properly cited.

© 2024 The Authors. *Carbon Energy* published by Wenzhou University and John Wiley & Sons Australia, Ltd.

1 | INTRODUCTION

The ever-extending demand for higher-energy-density batteries has prompted the investigation of state-of-the-art energy-storage systems to replace lithium-ion batteries.[1–6] Among the various secondary battery systems, lithium–sulfur batteries (LSBs) have been considered as attractive candidates for next-generation batteries to take the place of lithium-ion batteries thanks to their low price, eco-friendly nature, and high energy density (2600 Wh kg^{-1}), along with the abundance of sulfur resources in nature.[7–17] Despite the advantages of LSBs, their commercialization is limited by the shuttle reaction caused by the dissolution of lithium polysulfides (LPs) into the organic electrolyte during battery operation, which results in poor cycle performance and fast capacity fading.[18–27]

The most widely studied strategy for alleviating the LP shuttle effect is the confinement of LPs within rationally designed carbonaceous materials of various structures.[28–34] However, the limited adsorption ability of carbonaceous materials originating from weak van der Waals interactions between polar LPs and nonpolar carbonaceous materials hinders their application in LSBs. Transition-metal oxides (TMOs) can strongly anchor LPs via strong polar–polar chemical interactions owing to their hydrophilic surface properties and enhance the electrochemical kinetics of the LP conversion reaction by shortening long-chain LPs through the formation of metal–sulfur bonds, which reduces the S–S bonding strength in LPs. Furthermore, on the surface of TMOs, thiosulfate and polythionate ($[O_3S–S]^{2-}$ and $[O_3S_2–(S)_{x-2}–S_2O_3]$, respectively), which are widely known redox mediators in the LP transformation process, are formed via the catenation effect, which can accelerate the formation of short-chain LPs. Thus, various TMOs with good electrochemical performance have been proposed as new host materials for LSBs.[35–38] In contrast to carbonaceous materials, most studies on TMOs have focused on their chemical compositions in the case of strong interactions with LPs; with the exception of the hollow sphere structure, the morphology of TMOs has rarely been considered for cathode development in LSBs.[39] The LP anchoring ability of TMOs is significantly affected by their morphologies and compositions. Thus, the rational design of TMOs as cathode hosts for LSBs should consider both the composition and the structure of the TMO to optimize its LP anchoring ability.

Compared with the hollow sphere structure, the mesoporous structure has a much larger specific surface area, providing sufficient chemisorption sites for liquid LPs.[40–42] In addition, more LPs can be confined inside the mesoporous structure because of their unique structure. However, despite the advantages of mesoporous structures, few studies have been performed on TMOs with mesoporous structures in LSBs, to the best of our knowledge, owing to the difficulty of fabricating TMOs with mesoporous structures. Herein, we report TMOs with ordered mesoporous structures synthesized using a KIT-6-based template as a promising cathode host for LSBs with improved electrochemical performance. Three TMOs with ordered mesoporous structures (OM-Mn_2O_3, OM-Co_3O_4, and OM-NiO) were synthesized. Comparative analyses of OM-Co_3O_4 and OM-NiO revealed that OM-Mn_2O_3 was superior with regard to the LP anchoring ability and LP conversion kinetics. The strong chemisorption and fast conversion kinetics of LPs make OM-Mn_2O_3 a promising candidate for LP enclosures to effectively trap active sulfur species within the cathode, preventing the shuttle effect. Owing to the unique features of OM-Mn_2O_3, improved electrochemical performance of the LSB cell, including cycle and rate performance, was achieved by using the OM-Mn_2O_3/S composite as the cathode material. This study highlights the significance of the morphological structure and elemental composition of TMOs for the anchoring capacity and shuttle-effect prevention of LPs by clarifying the features of OM-Mn_2O_3 in LSB applications.

2 | EXPERIMENTAL SECTION

2.1 | Synthesis of mesoporous KIT-6 silica

KIT-6 (mesoporous silica) was synthesized using the method of Zheng et al.[29] First, 30 g of triblock copolymer Pluronic P-123 (poly(ethylene glycol)-block-poly(propylene glycol)-block-poly(ethylene glycol), molecular weight [MW] ≈ 5800; Sigma-Aldrich) was dissolved in deionized water, and 30 g of 1-butanol (>99.5%; Samchun) was added at 35°C. Subsequently, 59 g of HCl (37%; Samchun) and 64.5 g of tetraethyl orthosilicate (95.0%; Samchun), as the silica source, were added, followed by stirring for 24 h. Afterward, the mixture was subjected to aging in an oven at 100°C for 12 h. Subsequently, the resulting product was filtered and dried at 80°C. The silica product was then dispersed in an EtOH–HCl mixture, filtered several times using EtOH, and calcined at 550°C for 3 h in an atmosphere condition.

2.2 | Synthesis of mesoporous metal oxides (Mn_2O_3, Co_3O_4, and NiO)

Mesoporous TMOs (Mn_2O_3, Co_3O_4, and NiO) were prepared using a KIT-6 silica hard template. First,

26379368, 2024, 6, Downloaded from https://onlinelibrary.wiley.com/doi/10.1002/cey2.487 by Chung-Ang University, Wiley Online Library on [09/12/2024]. See the Terms and Conditions (https://onlinelibrary.wiley.com/terms-and-conditions) on Wiley Online Library for rules of use; OA articles are governed by the applicable Creative Commons License

7.71 g of manganese (II) nitrate hydrate ($Mn(NO_3)_2$; Aldrich), 12.46 g of cobalt (II) nitrate hexahydrate ($Co(NO_3)_2$; Alfa Aesar), and 12.98 g of nickel(II) nitrate hexahydrate ($Ni(NO_3)_2$; Aldrich), as precursors of Mn_2O_3, Co_3O_4, and NiO, respectively, were dissolved at 100°C. Next, the solutions were impregnated into the pores of silica templates, and the mixtures were heat-treated. After the heat treatment, the products were calcined at 200°C and 550°C for 1 and 3 h, respectively. Finally, the silica templates were removed with a 2 M sodium hydroxide (NaOH, 98.0%; Samchun) aqueous solution several times and washed with deionized water. After drying, dark-gray mesoporous TMOs (Mn_2O_3, Co_3O_4, and NiO) were obtained.

2.3 | Preparation of OM-TMO/S composites (OM-Mn_2O_3/S, OM-Co_3O_4/S, OM-NiO/S)

The TMOs with ordered mesoporous structures (OM-Mn_2O_3, OM-Co_3O_4, and OM-NiO) were uniformly mixed with sulfur using a mortar at a mass ratio of 2:3. The resulting powder was transferred to a vial and placed in a Teflon autoclave. Then, the powders were heated at 155°C for 12 h, following a typical sulfur melt-diffusion method.

2.4 | Preparation of polysulfide solution (Li_2S_6 solution)

Lithium sulfide (Li_2S, 99.9%; Alfa Aesar) and sulfur powder at a molar ratio of 1:5 were dissolved in appropriate amounts of 1,3-dioxolane (DOL)/1,2-dimethoxyethane (DME) (1:1 volume ratio) solution with the polysulfide. The obtained solution was stirred for 24 h in a glovebox.

2.5 | Characterization

X-ray diffraction (XRD) (PANalytical EMPYREAN) was used to estimate the crystal structures of the synthesized materials. Transmission electron microscopy (TEM) (JEOL ARM-200F) was used to determine the pore structures of the OM-TMOs and elemental sulfur infiltration. The N_2 adsorption/desorption isotherms were measured using the Micromeritics ASAP 2460 instrument (Micromeritics Instrument Corp.) at a temperature maintained by liquid nitrogen. The pore-diameter distributions and specific surface areas of the materials were calculated using the Brunauer–Emmett–Teller (BET) and Barrett–Joyner–Halenda equations, respectively. Ultraviolet–visible (UV–vis) spectroscopy was performed using a UV–vis spectrophotometer for further analysis of the polysulfide adsorption. X-ray photoelectron spectroscopy (XPS) (Thermo Fisher Scientific USA ESCALAB-250) was used to characterize the sample surfaces. The weight ratios of sulfur in the metal oxide/S composites were determined via thermogravimetric analysis (TGA) (Scinco N-1000).

2.6 | Cell assembly and electrochemical measurements

To prepare the cathode electrode, the active materials (OM-Mn_2O_3/S, OM-Co_3O_4/S, OM-NiO/S), Ketjenblack (KB) (EC-600JD carbon black; Akzo Nobel), and poly(ethylene oxide) (PEO, MW ≈ 1,000,000; Aldrich) were uniformly mixed at a mass ratio of 60:20:20 and dispersed in an acetonitrile (99.8%; Aldrich) solvent using a Thinky mixer (2000 rpm, 15 min, three times). The slurry was cast on an aluminum-foil current collector and dried for 12 h at 60°C. Next, the cathode was stamped to 12 mm (in diameter) with a sulfur-loading level of 1.8–2.0 mg cm^{-2}. A lithium metal foil with a diameter of 14 mm was used as the anode, and W-scope PE (18 mm in diameter) was used as the separator. Next, CR2032 coin cells were assembled with an electrolyte consisting of 1 M bis(trifluoromethane) sulfonimide lithium salt (LiTFSI, 99.95%; Aldrich) and 0.4 M lithium nitrate ($LiNO_3$, 99.98%; Alfa Aesar) in a mixed solvent of DOL/DME (volume ratio of 1:1) in a glovebox for electrochemical measurements. Each coin cell was fabricated with an electrolyte/sulfur ratio of 30 μL/mg. Galvanostatic charge/discharge cycling was performed in the voltage range of 1.8–2.6 V. Cyclic voltammetry (CV) was conducted at voltages ranging from 1.6 to 2.8 V at a scan rate of 0.1 mV s^{-1}. Electrochemical impedance spectroscopy (EIS) was performed using VMP3 (BioLogic) in the frequency range of 100 kHz to 10 MHz.

2.7 | Preparation of polysulfide solution (Li_2S_6, Li_2S_8 solution)

Lithium sulfide (Li_2S, 99.9%; Alfa Aesar) and sulfur powder at a molar ratio of 1:5 for Li_2S_6 and 1:7 for Li_2S_8 were dissolved in appropriate amounts of DOL/DME (1:1 volume ratio) solution, followed by stirring for 24 h in a glovebox.

2.8 | Polysulfide adsorption test

To verify the adsorption ability of the OM-TMOs, the Li_2S_6 adsorption test was conducted in a glovebox; 6 mL

26379368, 2024, 6, Downloaded from https://onlinelibrary.wiley.com/doi/10.1002/cey2.487 by Chung-Ang University, Wiley Online Library on [09/12/2024]. See the Terms and Conditions (https://onlinelibrary.wiley.com/terms-and-conditions) on Wiley Online Library for rules of use; OA articles are governed by the applicable Creative Commons License

of the prepared 3 mM Li_2S_6 solution was added to the vial with 6 mg of OM-TMOs powders for 24 h.

2.9 | Cell assembly of the Li_2S_6 symmetric cell for CV

To investigate the catalytic effect, CV was performed on the Li_2S_6 symmetric cells. Both the electrodes of each symmetric cell were composed of the same type of OM-TMO (OM-Mn_2O_3, OM-Co_3O_4, or OM-NiO) and KB at a mass ratio of 3:1. Identical electrodes with diameters of 14 mm and a PE separator with a diameters of 18 mm, and 60 μL of 0.25 M Li_2S_6 with 1 M LiTFSI in DOL/DME (volume ratio of 1:1) as the electrolyte were assembled. Each cell was swept between −0.8 and 0.8 V at a scan rate of 1 mV s^{-1}.

2.10 | Precipitation and dissolution test of Li_2S

The coin cell was assembled with a OM-TMOs/KB electrode (with a 12 mm diameter) as the cathode, a PE separator with a diameter of 18 mm, and a lithium metal foil with a diameter of 14 mm as the anode. A total of 20 μL of 0.25 M Li_2S_8 with 1 M LiTFSI solution, and the same amount of conventional electrolyte was added to the cathode and anode. The coin cells were first discharged to 2.14 V and then discharged at a constant voltage of 2.09 V. In contrast, for the Li_2S dissolution test, the coin cells were fully discharged to 1.8 V, followed by a charging step at a constant voltage of 2.4 V until the current was <0.01 mA.

2.11 | Density functional theory (DFT) calculations

Ab initio calculations were performed utilizing the projector-augmented wave implemented in the Cambridge Sequential Total Energy Package. Generalized gradient approximation with the Perdew–Burke–Ernzerhof method was used for exchange-correlation functional parameterization. The metal-oxide surfaces of Mn_2O_3, Co_3O_4, and NiO were selected as (111), (400), and (200), respectively. The cleavage of the metal-oxide surfaces was modeled using the geometry tool in BIOVIA Material Studio 2021. The Li_2S_6 molecules were relaxed on the metal surfaces. The adsorption energies of Li_2S_6 on the metal surfaces were calculated as follows:

$$\Delta E_{ad} = E_{Li_2S_6-sub} - [E_{sub} + E_{Li_2S_6}], \quad (1)$$

where $E_{Li_2S_6-sub}$, E_{sub}, and $E_{Li_2S_6}$ represent the total free energies of adsorbed Li_2S_6 on the metal oxides, metal substrates, and Li_2S_6 molecules, respectively. The charge–density differences were calculated using the following equation:

$$\Delta\rho = \rho_{Li_2S_6-sub} - \rho_{sub} - \rho_{composite}, \quad (2)$$

where $\rho_{Li_2S_6-sub}$, ρ_{sub}, and $\rho_{Li_2S_6}$ represent the charge densities of the Li-adsorbed metal oxides, metal-oxide substrates, and Li_2S_6 molecules in the same configuration, respectively.

3 | RESULTS AND DISCUSSION

3.1 | Physicochemical characterization analysis of TMOs with ordered mesoporous structures

As illustrated in Figure 1A, three TMOs with ordered mesoporous structures—Mn_2O_3, Co_3O_4, and NiO—were synthesized using KIT-6. To confirm the successful synthesis of TMOs with an ordered mesoporous structure (OM-TMO), the pore and crystal structures of the prepared OM-TMOs were analyzed using XRD. As shown in Figure 1B, (211) and (332) low-angle diffraction peaks were observed, indicating that the TMOs had an ordered mesoporous structure similar to that of KIT-6 (Figure S1). Furthermore, the (110) peak that appeared after removing the template was attributed to the phase transition to the lower space group, which occurred during the calcination of the transition-metal precursor after it filled the two pore channels of KIT-6 (where only one chiral channel was used).[43–45] As indicated by the wide-angle XRD patterns in Figure 1B, the crystal structures of the TMOs matched the general crystalline phases of Mn_2O_3 (JCPDS No. 41-1442), Co_3O_4 (JCPDS No. 42-1467), and NiO (JCPDS No. 47-1049).[43,46,47] According to the XRD analysis, the synthesized materials were Mn_2O_3, Co_3O_4, and NiO with ordered mesoporous structures (denoted as OM-Mn_2O_3, OM-Co_3O_4, and OM-NiO, respectively), which was confirmed via scanning electron microscopy and energy-dispersive X-ray spectroscopy (EDS) mapping of the three prepared materials (Figure S2). Moreover, N_2 adsorption and desorption tests were conducted to verify the specific surface areas and pore volumes of the synthesized OM-TMOs. As shown in Figures 1C and S3, the isotherm curves of OM-Mn_2O_3, OM-Co_3O_4, OM-NiO, and KIT-6 were type-IV, with hysteresis loops in the relative pressure (P/P_0) range of 0.6–1.0, which is a feature of mesoporous materials.[48]

26379368, 2024, 6, Downloaded from https://onlinelibrary.wiley.com/doi/10.1002/cey2.487 by Chung-Ang University, Wiley Online Library on [09/12/2024]. See the Terms and Conditions (https://onlinelibrary.wiley.com/terms-and-conditions) on Wiley Online Library for rules of use; OA articles are governed by the applicable Creative Commons License

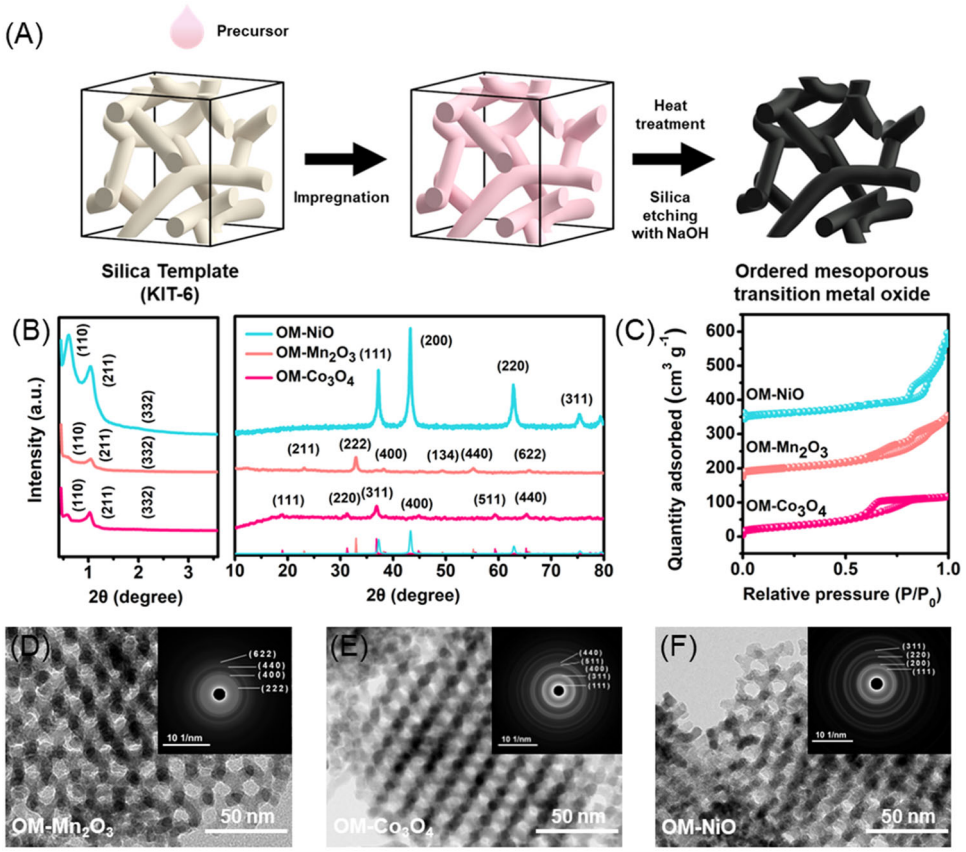


FIGURE 1 (A) Procedure for synthesizing ordered mesoporous TMO. (B) XRD pattern, (C) N_2 adsorption/desorption curves, and (D–F) TEM images and SAED patterns of OM-Mn_2O_3, OM-Co_3O_4, and OM-NiO.

The specific surface areas and pore volumes of OM-Mn_2O_3, OM-Co_3O_4, and OM-NiO were measured to be 112 $m^2 g^{-1}$ and 0.24 $cm^3 g^{-1}$ (OM-Mn_2O_3), 106 $m^2 g^{-1}$ and 0.18 $cm^3 g^{-1}$ (OM-Co_3O_4), and 45 $m^2 g^{-1}$ and 0.14 $cm^3 g^{-1}$ (OM-NiO), respectively. The pore-diameter distributions of OM-Mn_2O_3, OM-Co_3O_4, and OM-NiO revealed two types of pore sizes (Figure S4), indicating a bimodal pore structure. Furthermore, high-resolution TEM images and selected area electron diffraction (SAED) patterns confirmed that the OM-TMOs (OM-Mn_2O_3, OM-Co_3O_4, and OM-NiO) were successfully synthesized as ordered mesoporous structures with pore sizes of 2–20 nm (Figure 1D–F).

A visualized LP (Li_2S_6) adsorption test was performed by adding OM-Mn_2O_3, OM-Co_3O_4, or OM-NiO powder (3 mg) to a Li_2S_6 solution (6 mL, 3 mM) for 24 h to evaluate the Li_2S_6 adsorption capacity of the OM-TMOs. As shown in the inset of Figure 2A, the original color of the Li_2S_6 solution was somber yellow. When OM-NiO and OM-Co_3O_4 were added to the Li_2S_6 solution, its color did not change significantly even after soaking for 24 h, and OM-NiO showed inferior Li_2S_6 adsorption to the other two samples. However, after soaking OM-Mn_2O_3 in the solution for 24 h, the color of the Li_2S_6 solution turned transparent from the original somber yellow color of the Li_2S_6 solution, indicating that Li_2S_6 was completely absorbed by OM-Mn_2O_3. The highest Li_2S_6 anchoring capacity of OM-Mn_2O_3 was confirmed through UV–vis spectral analysis. As shown in Figure 2A, the distinguishable peak intensity in the range from 250 to 300 nm, attributed to the presence of Li_2S_6, increases in the order of OM-Mn_2O_3 < OM-Co_3O_4 < OM-NiO < Li_2S_6, suggesting that OM-Mn_2O_3 is an effective LP absorber.[49]

According to the catenation effect, when long-chain LPs (Li_2S_x, $2 < x \leq 8$) come into contact with a TMO, thiosulfate ($S_2O_3^{2-}$) and polythionate ($[O_3S_2–(S)_x–S_2O_3]^{2-}$) are formed on the TMO surface, reducing their oxidation numbers.[50] Additionally, thiosulfate—a redox mediator in LSBs—converts long-chain LPs into short-chain LPs (or vice versa). XPS analysis was conducted to demonstrate the catenation effect of the OM-TMOs. In the XPS S 2p spectra of Li_2S_6 (Figure 2B), two peaks at 163.1 and 161.6 eV corresponding to bridge sulfur (S_B^0) and terminal sulfur (S_T^{-1}), respectively, were observed; the intensity ratio of S_B^0:S_T^{-1} was 2:1. These peaks are related to the chain structure of Li_2S_6, where the sulfur atoms at both ends had a charge of –1, whereas those in the middle had a charge of 0.[51,52] After the Li_2S_6 adsorption test, the solid

26379368, 2024, 6, Downloaded from https://onlinelibrary.wiley.com/doi/10.1002/cey2.487 by Chung-Ang University, Wiley Online Library on [09/12/2024]. See the Terms and Conditions (https://onlinelibrary.wiley.com/terms-and-conditions) on Wiley Online Library for rules of use; OA articles are governed by the applicable Creative Commons License

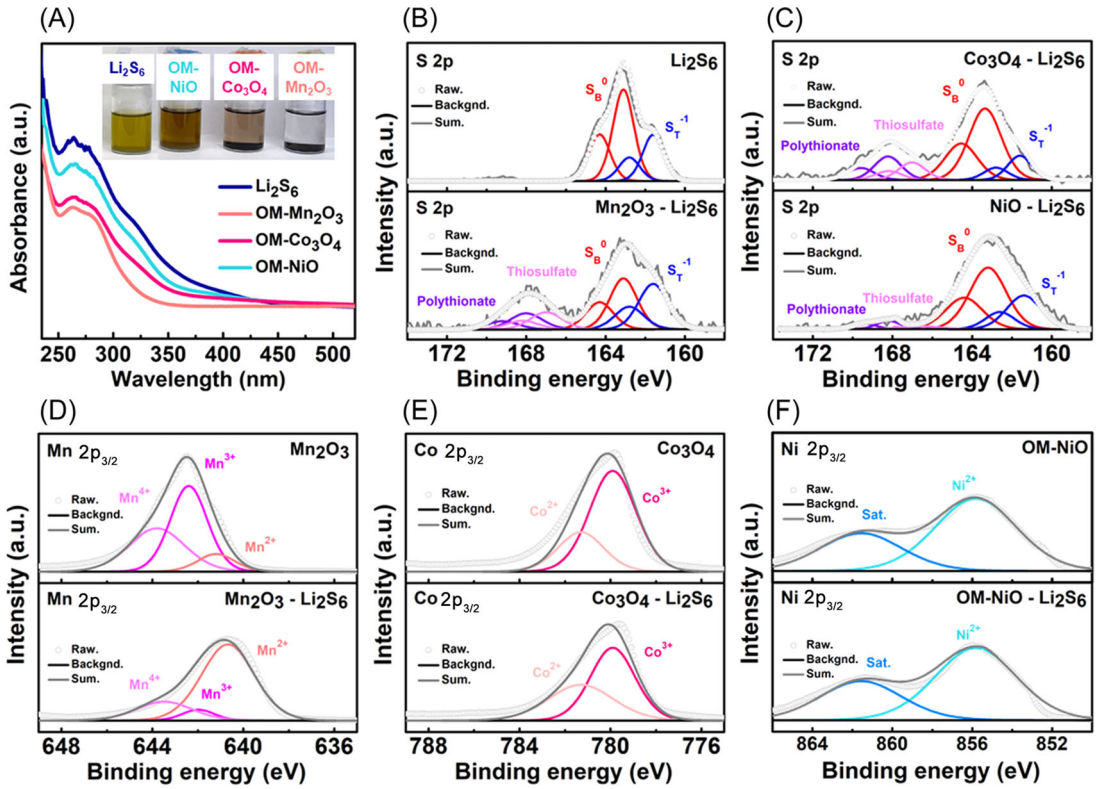


FIGURE 2 (A) Optical images of the LP anchoring test and UV–vis data of OM-Mn_2O_3, OM-Co_3O_4, and OM-NiO in the 3 mM Li_2S_6 solution. (B, C) S 2p, (D) Mn 2p, (E) Co 2p, and (F) Ni 2p XPS spectra before and after the Li_2S_6 adsorption test.

residues remaining on the surfaces of OM-Co_3O_4 and OM-NiO were identified as Li_2S_6, and the ratio of S_B^0:S_T^{-1} was approximately 2:1 (Figure 2B,C). Therefore, OM-Co_3O_4 and OM-NiO showed weak chemical interactions with Li_2S_6. Owing to the weak chemical interactions of Li_2S_6 with OM-Co_3O_4 and OM-NiO, the valence states of Co and Ni changed slightly, as indicated by the Co $2p_{3/2}$ and Ni $2p_{3/2}$ XPS spectra. Moreover, there were two weak S 2p peaks at 168.2 and 169.2 eV, which were indexed to thiosulfate ($S_2O_3^{2-}$) and polythionate ($[O_3S_2–(S)_x–S_2O_3]^{2-}$), respectively (Figure 2D–F).[50] However, the solid residue on the surface of OM-Mn_2O_3 was identified as Li_2S_4, with an S_B^0:S_T^{-1} ratio of 1:1. The reduced fraction of S_B^0 for OM-Mn_2O_3 indicated the oxidization of Li_2S_6 to Li_2S_4, suggesting that more thiosulfate and polythionate were produced. This resulted from the electron transfer from Li_2S_6 to OM-Mn_2O_3. Thus, the contribution of Mn^{2+} (641.2 eV) to the Mn $2p_{3/2}$ XPS spectrum increased significantly, whereas the contributions of Mn^{3+} and Mn^{4+} (642.4 and 643.8 eV) in the Mn $2p_{3/2}$ XPS spectrum decreased (Figure 2D–F).[53] Consequently, the Mn $2p_{3/2}$ XPS spectrum was shifted by 1.6 eV toward a lower binding energy, and two S 2p peaks appeared at 168.2 and 169.2 eV, which were indexed to thiosulfate ($S_2O_3^{2-}$) and polythionate ($[O_3S_2–(S)_x–S_2O_3]^{2-}$), respectively. According to the results, OM-Mn_2O_3, which shows high reactivity with LPs, can be considered to be the most effective cathode host material among the prepared OM-TMOs.

To theoretically corroborate the affinity of Li_2S_6 for metal oxides, the surface adsorption energies of Li_2S_6 on Mn_2O_3, Co_3O_4, and NiO were calculated using DFT. The optimized structures for the adsorption of Li_2S_6 on the Mn_2O_3, Co_3O_4, and NiO surfaces are illustrated in Figure 3A–C. The adsorption energy of Li_2S_6 (−2.3644 eV) on Mn_2O_3 was higher than those for Co_3O_4 and NiO (Figure 3D). The Mn-terminated surface bonded with Li_2S_6, and electrons were fully transferred from Li_2S_6 to Mn_2O_3. In contrast, Co_3O_4 and NiO showed less electron transfer from Li_2S_6, which is represented by excess electrons near the Li–O bond (yellow isosurface) in Figure 3B,C. Notably, Mn can store more electrons transferred from Li_2S_6 than Co and Ni. Bader charge analysis confirmed that the net charge of Mn below the Li_2S_6 molecules was +1.67e, which was a relatively positive charge state compared with those of Co (+1.28e) and Ni (+1.03e). The average net charge of Mn on the Mn_2O_3 surface was +1.28e. The amount of charge transferred was 0.2e. In comparison, Co and Ni showed smaller amounts of charge transfer: 0.13e and 0.15e, respectively. According to the DFT calculations, Mn_2O_3 had a high affinity to Li_2S_6, and it can prevent the shuttle effect by efficiently anchoring LPs during cell operation.

26379368, 2024, 6, Downloaded from https://onlinelibrary.wiley.com/doi/10.1002/cey2.487 by Chung-Ang University, Wiley Online Library on [09/12/2024]. See the Terms and Conditions (https://onlinelibrary.wiley.com/terms-and-conditions) on Wiley Online Library for rules of use; OA articles are governed by the applicable Creative Commons License

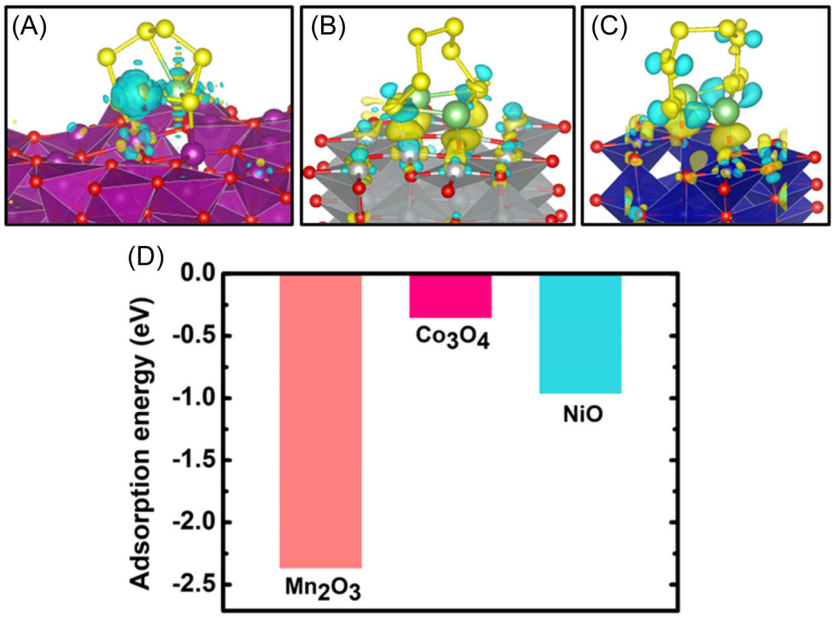


FIGURE 3 Optimized structures and charge-density differences after Li_2S_6 adsorption on the (A) (222) surface of Mn_2O_3, (B) (400) surface of Co_3O_4, and (C) (200) surface of NiO. (D) Calculated adsorption energy of Li_2S_6 on the TMOs.

3.2 | Characterization of OM-TMO/sulfur composites

OM-TMO/S composites (OM-Mn_2O_3/S, OM-Co_3O_4/S, and OM-NiO/S) were prepared as cathode materials using the melt-diffusion method.[54] XRD analysis, BET analysis, TGA, TEM, and EDS were performed to confirm the entry of sulfur into the OM-TMOs. In Figure 4A, the reduced peak intensity of sulfur between 20° and 30° in the XRD pattern indicates the successful entry of sulfur species into the pores of the OM-TMOs with ordered mesoporous structures (OM-Mn_2O_3, OM-Co_3O_4, and OM-NiO).[55,56] Furthermore, the BET curves of the OM-Mn_2O_3/S, OM-Co_3O_4/S, and OM-NiO/S composites shown in Figure 4B indicated reduced adsorption volumes without hysteresis loops, implying that sulfur filled the space of OM-TMOs. TGA was conducted to determine the mass contents of sulfur in the OM-TMO/S composites. As shown in Figure 4C, no further weight loss was observed after the temperature reached approximately 250°C, indicating that the sulfur content in the OM-TMOs was 60 wt%. The OM-TMO/S composites were analyzed using TEM to confirm the uniform sulfur loading in the pores of the OM-TMOs. As shown in Figure 4D–F, nonporous structures can be seen in the TEM images of the OM-TMO/S composites, which is because the sulfur species filled the mesopores of the OM-TMOs. Moreover, from the EDS elemental mapping of Mn, Co, Ni, O, and S, sulfur was found to be uniformly distributed in all the TMO/sulfur composites; thus, well-designed cathode materials (OM-Mn_2O_3/S, OM-Co_3O_4/S, and OM-NiO/S) were successfully synthesized.

3.3 | Catalytic effect of OM-TMO/sulfur composite electrodes

CV was performed by applying a voltage scan rate of 0.1 mV s^{-1} within the voltage range of 1.6–2.8 V to evaluate the electrochemical reactivity of the OM-TMOs/S composites. The three initial cycles of the CV curves for pristine sulfur, OM-Mn_2O_3/S, OM-Co_3O_4/S, and OM-NiO/S electrodes are shown in Figure 5A–D. During the reduction process, two peaks were observed at approximately 2.3 and 2.0 V, which are attributed to the consecutive reduction of elemental sulfur (S_8) to soluble Li_2S_x ($2 < x \leq 8$) and Li_2S/Li_2S_2.[57,58] In contrast, the distinct peak before 2.4 V in the oxidation state resulted from the oxidation of insoluble Li_2S/Li_2S_2 to Li_2S_8/S_8. For the pristine sulfur electrode, the anodic peak occurred at the highest voltage of 2.39 V, and the reduction peaks occurred at 2.01 and 2.27 V. Furthermore, the sweep in the cell with pristine sulfur electrodes showed lower reversibility from the initial cycle to the third cycle. The OM-TMO/S composite electrode had a lower oxidation peak and higher reduction peaks than pristine sulfur electrode, indicating that the overpotential for the LP electrochemical reaction decreased and the redox kinetics was accelerated. The OM-Mn_2O_3/S electrode showed the highest redox activity and reversibility among the electrodes. This is consistent with the presence of thiosulfate and polythionate, which are well-known redox mediators of LPs, on the TMOs.[50] On the basis of the results of CV tests, it was found that all the OM-TMOs/S composites showed better reversibility than the pristine sulfur electrode.

26379368, 2024, 6, Downloaded from https://onlinelibrary.wiley.com/doi/10.1002/cey2.487 by Chung-Ang University, Wiley Online Library on [09/12/2024]. See the Terms and Conditions (https://onlinelibrary.wiley.com/terms-and-conditions) on Wiley Online Library for rules of use; OA articles are governed by the applicable Creative Commons License

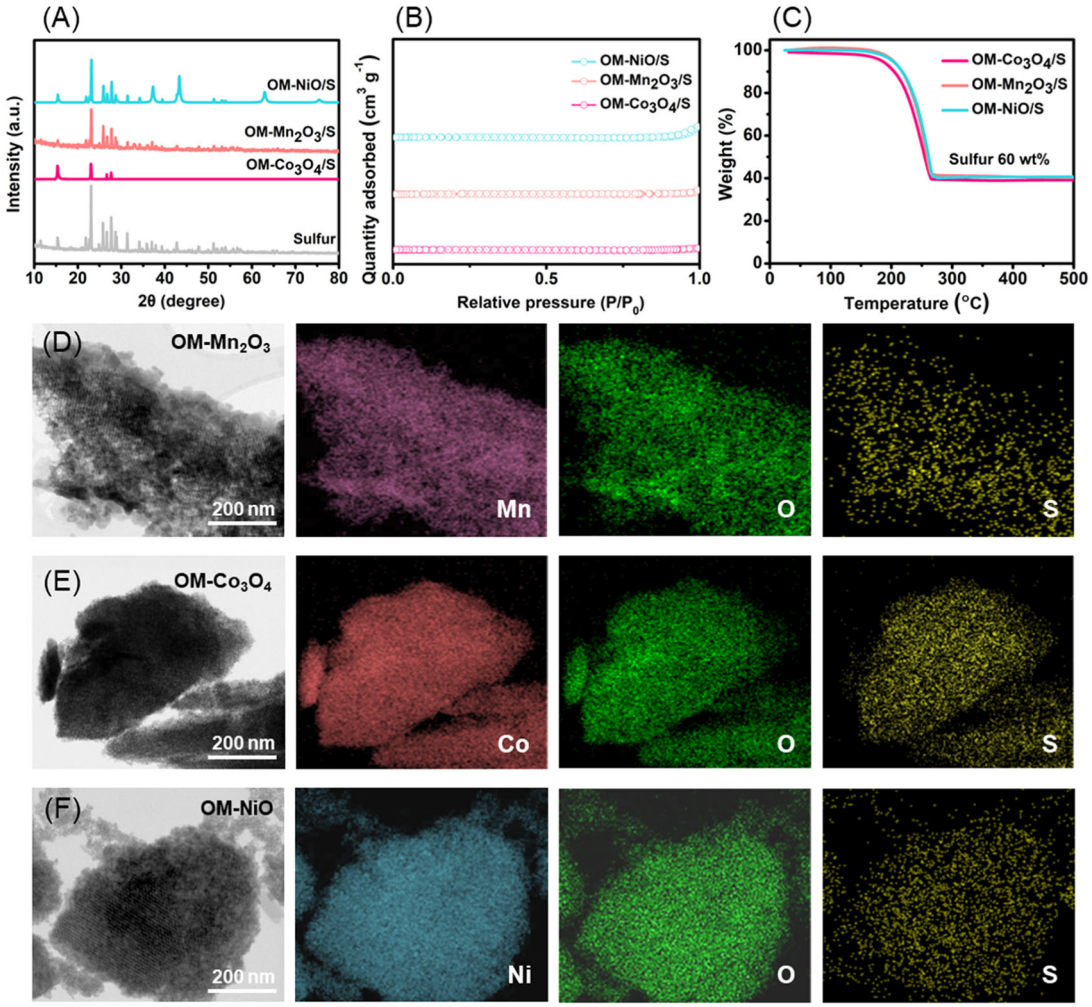


FIGURE 4 (A) XRD patterns of sulfur and OM-Mn_2O_3/S, OM-Co_3O_4/S, and OM-NiO/S. (B) N_2 adsorption/desorption curves, (C) TGA curves, and (D–F) TEM and EDS images of OM-Mn_2O_3/S, OM-Co_3O_4/S, and OM-NiO/S.

To adequately explain the enhanced conversion kinetics and reversibility, the catalytic effect of OM-TMOs on the LP conversion reaction was explored using symmetric cells containing Li_2S_6 solutions with working and counter electrodes of the following types: (1) KB, (2) OM-Mn_2O_3/KB, (3) OM-Co_3O_4/KB, and (4) OM-NiO/KB. As shown in Figure 5E–H, OM-Mn_2O_3/KB showed the highest peak current and two distinct pairs of peaks representing solid–liquid (Li_2S–Li_2S_6) and liquid–solid (Li_2S_6–S_8) redox reactions. These results indicated that OM-Mn_2O_3 had the highest catalytic activity and boosted the conversion kinetics of the LPs.

To further evaluate the positive effect of OM-TMOs, particularly for the Li_2S redox reaction, which contributed 75% of the overall capacity, Li_2S nucleation and dissolution tests were performed using the potentiostatic charge and discharge process. As shown in Figure 5I–L, the OM-Mn_2O_3/KB electrode took the shortest time to reach the peak current, suggesting that the kinetics of Li_2S precipitation from soluble LPs was accelerated. Additionally, the capacity contribution of deposited Li_2S was 176 mA h g_s^{-1} for the OM-Mn_2O_3/KB electrode, which was the highest among the prepared electrodes. In the case of the oxidation of the deposited Li_2S to soluble LPs, the OM-Mn_2O_3/KB electrode took the shortest time to reach the peak current and showed the largest capacity contribution[59,60] (Figure 5M–P).

The accelerated reaction kinetics related to Li_2S reduction and oxidation were supported by galvanostatic intermittent titration technique analysis at a C-rate of 0.03 C (Figure S5). The calculation of internal resistance at various lithiation/delithiation stages was performed utilizing the following equation:

$$\Delta R \quad (\Omega) = \frac{|V_{QOCV} - V_{CCV}|}{I_{applied}}, \tag{3}$$

where V_{QOCV}, V_{CCV}, and $I_{applied}$ represent the quasi-open-circuit voltage, closed-circuit voltage, and applied

26379368, 2024, 6, Downloaded from https://onlinelibrary.wiley.com/doi/10.1002/cey2.487 by Chung-Ang University, Wiley Online Library on [09/12/2024]. See the Terms and Conditions (https://onlinelibrary.wiley.com/terms-and-conditions) on Wiley Online Library for rules of use; OA articles are governed by the applicable Creative Commons License

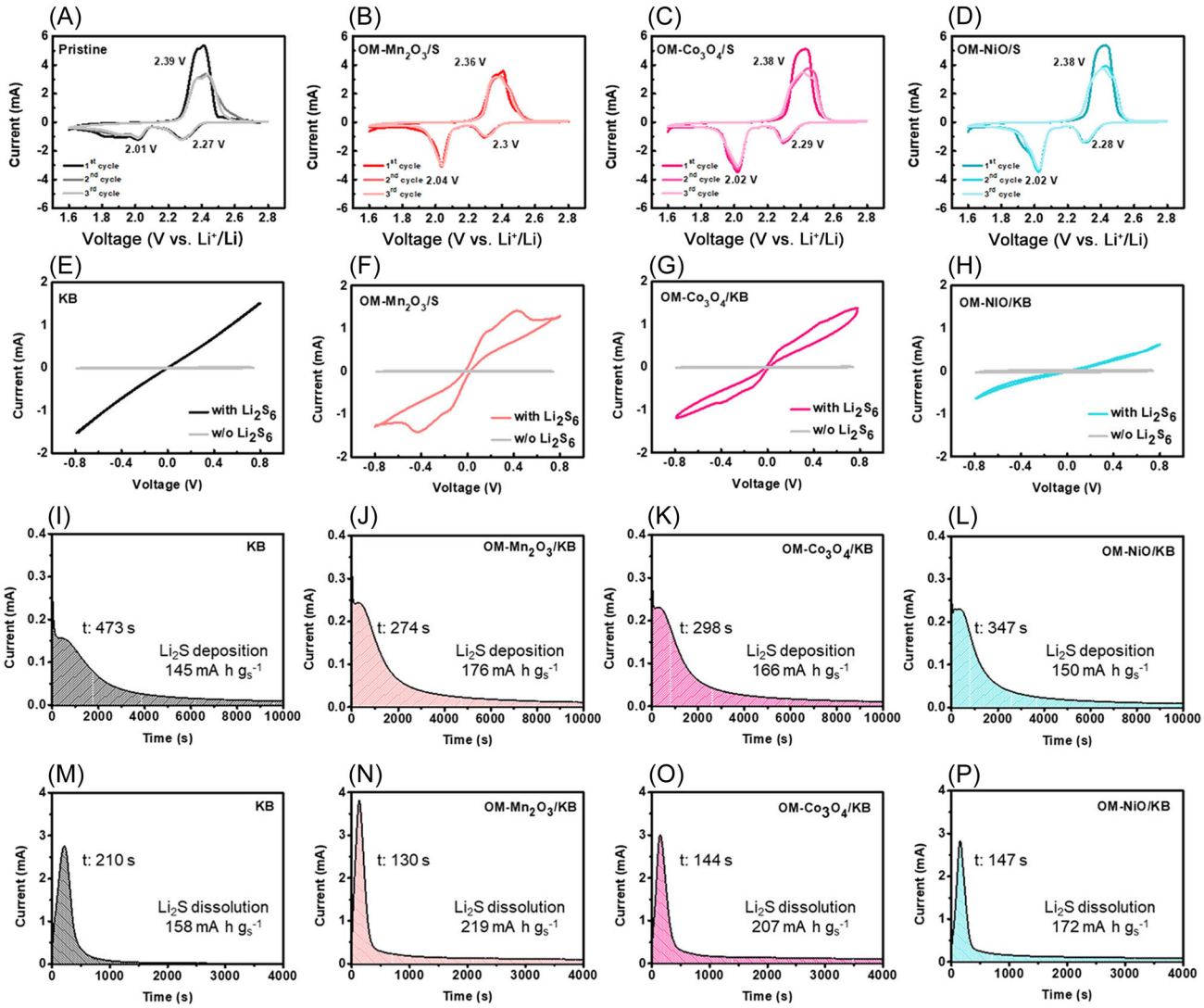


FIGURE 5 CV curves of (A) pristine sulfur, (B) OM-Mn_2O_3/S, (C) OM-Co_3O_4/S, and (D) OM-NiO/S electrodes in the potential range of 1.6–2.8 V (vs. Li^+/Li) acquired at a scan rate of 0.1 mV s^{-1}. (E–H) CV curves of the Li_2S_6 symmetric cell with various electrodes. (I–L) Potentiostatic discharge profiles of Li_2S_8 on various electrodes at 2.09 V. (M–P) Potentiostatic charge profiles of Li_2S_8 on different electrodes at 2.4 V.

current, respectively. After the nucleation of Li_2S at 25% depth of discharge (DOD), the internal resistance sharply increased at 70% DOD, corresponding to Li_2S growth, because the reaction kinetics slowed significantly as the Li_2S began to wrap around the electrode.[61] Eventually, the internal resistance was maximized when the Li–S cell was fully discharged for all four electrodes, because Li_2S with insulating properties fully covered the entire electrode. Additionally, in the charging step of the Li–S cells, the internal resistance started to decrease after reaching the initial peak related to the activation of the deposited Li_2S on the electrode. For both the discharging and charging states, the OM-Mn_2O_3/S electrode showed the lowest internal resistance associated with Li_2S growth and activation. According to the results, OM-Mn_2O_3 expedites the conversion of soluble LPs into Li_2S and vice versa. Therefore, we believe that OM-Mn_2O_3 has a bidirectional catalytic ability, allowing the reversible reaction of sulfur species.

3.4 | Electrochemical performance of OM-TMO/sulfur composite electrodes

The electrochemical performance of the Li–S cells assembled with pristine sulfur, OM-Mn_2O_3/S, OM-Co_3O_4/S, and OM-NiO/S electrodes was assessed (Figure 6). The galvanostatically cycled voltage profiles obtained with a C-rate of 0.5 C were compared at the first cycle (Figure 6A) and the 100th cycle (Figure 6B).

26379368, 2024, 6, Downloaded from https://onlinelibrary.wiley.com/doi/10.1002/cey2.487 by Chung-Ang University, Wiley Online Library on [09/12/2024]. See the Terms and Conditions (https://onlinelibrary.wiley.com/terms-and-conditions) on Wiley Online Library for rules of use; OA articles are governed by the applicable Creative Commons License

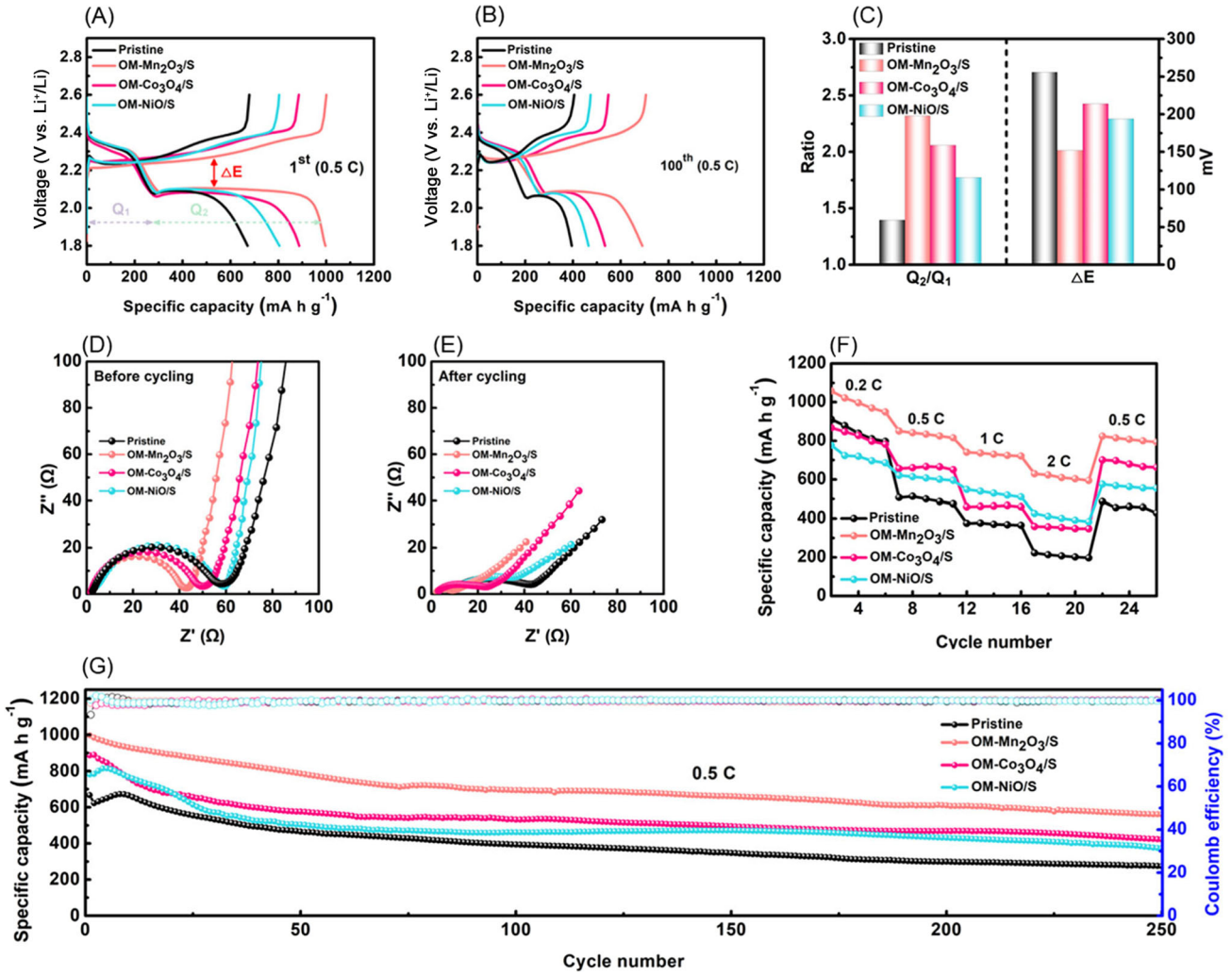


FIGURE 6 Electrochemical performance of Li–S cells with pristine sulfur, OM-Mn_2O_3/S, OM-Co_3O_4/S, and OM-NiO/S electrodes. Charge/discharge voltage profiles of the (A) first cycle and (B) 100th cycle at 0.5 C. (C) Q_2/Q_1 and ΔE values from the first-cycle charge/discharge voltage profiles. EIS results (D) before cycling and (E) after 100 cycles. (F) Performance at different C rates. (G) Performance over 250 cycles.

As shown in Figure 6A, the Li–S cell with the pristine sulfur electrode had a specific discharge capacity of 671 mA h g^{-1} in the first cycle. On the other hand, the Li–S cells with OM-Mn_2O_3/S, OM-Co_3O_4/S, and OM-NiO/S electrodes showed discharge capacities of 998, 887, and 804 mA h g^{-1}, respectively, in the first cycle. In the discharge process, two plateaus were observed, corresponding to $S_8 \rightarrow Li_2S_4$ (4-electron reaction, upper plateau, denoted as Q_1) and $Li_2S_4 \rightarrow Li_2S$ (12-electron reaction, lower plateau, denoted as Q_2).[62] Because the shuttle reaction caused by soluble LPs and the sluggish transition kinetics of LPs reduce Q_1 and Q_2, the capacity ratio of Q_2 to Q_1 represents the catalytic activity in the LP conversion process. The Q_2/Q_1 value of OM-Mn_2O_3/S was 2.32, which was the highest among the prepared electrodes (pristine: 1.396; OM-Co_3O_4/S: 2.058; OM-NiO/S: 1.773), indicating that the OM-Mn_2O_3 enhanced the catalytic ability for the LP conversion reaction. Furthermore, the OM-Mn_2O_3/S electrode showed less polarization (ΔE) between the charge and discharge processes than the pristine (256 mV), OM-Co_3O_4/S (214 mV), and OM-NiO/S (194 mV) electrodes, which mainly originated from the reduced charge-transfer resistance and the accelerated activation kinetics of Li_2S (Figures 6D and S6). Even after 100 cycles, the discharge capacities of the Li–S cells with the OM-TMO/S composite electrodes (OM-Mn_2O_3/S electrode: 678 mA h g^{-1}; OM-Co_3O_4/S electrode: 534 mA h g^{-1}; OM-NiO/S electrode: 465 mA h g^{-1}) were higher than that of the Li–S cell with the pristine sulfur electrode (394 mA h g^{-1}). This is because the OM-TMO/S composite electrode accelerated the charge transfer and suppressed the LP dissolution compared with the pristine sulfur electrode (Figure 6E,F).

26379368, 2024, 6, Downloaded from https://onlinelibrary.wiley.com/doi/10.1002/cey2.487 by Chung-Ang University, Wiley Online Library on [09/12/2024]. See the Terms and Conditions (https://onlinelibrary.wiley.com/terms-and-conditions) on Wiley Online Library for rules of use; OA articles are governed by the applicable Creative Commons License

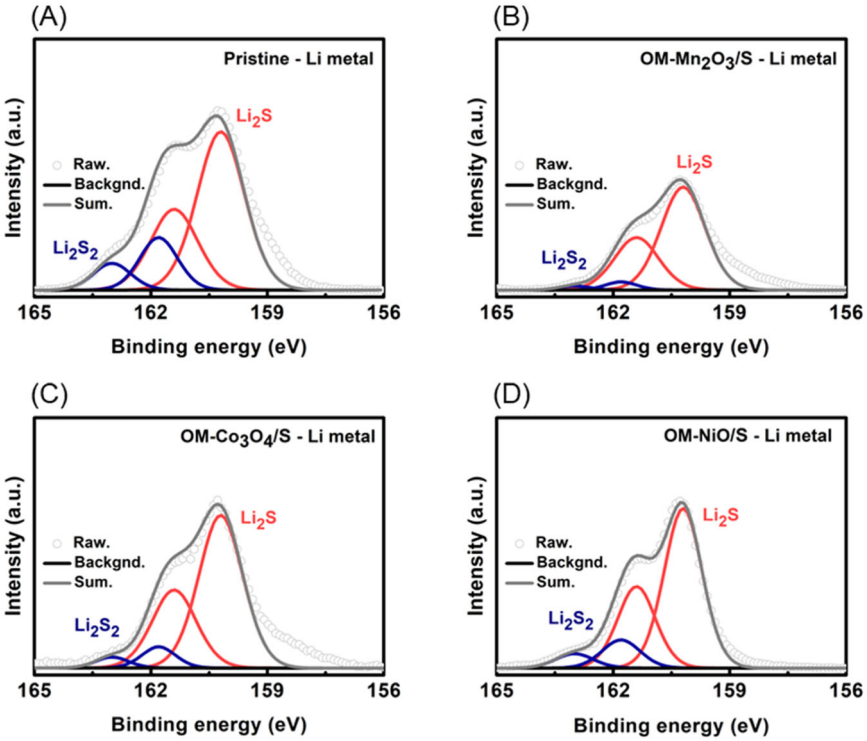


FIGURE 7 XPS S 2p spectra of a lithium metal anode assembled with (A) pristine sulfur, (B) OM-Mn_2O_3/S, (C) OM-Co_3O_4/S, and (D) OM-NiO/S electrodes after cycling.

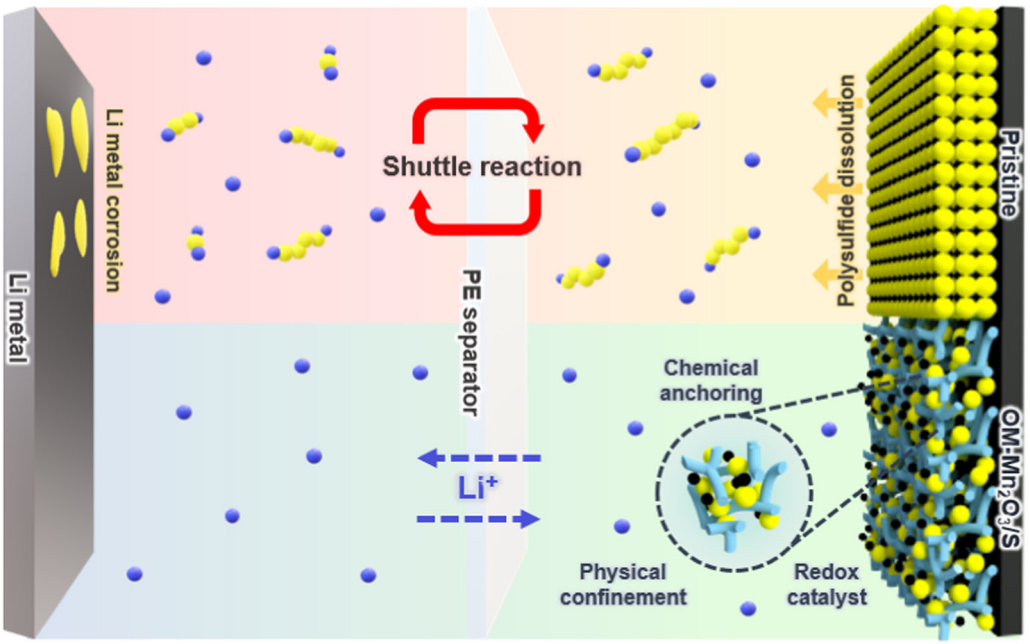


FIGURE 8 Schematic of the Li–S cell equipped with pristine sulfur and OM-Mn_2O_3/S electrodes.

The highest capacity retention and the lowest voltage polarization of the OM-Mn_2O_3/S electrodes can be logically explained by the combined effect of the strong chemical interaction of OM-Mn_2O_3 with the LPs and the enhanced redox reaction of OM-Mn_2O_3. The rate performance of Li–S cells with pristine sulfur, OM-Mn_2O_3/S, OM-Co_3O_4/S, and OM-NiO/S electrodes at current densities from 0.2 to 2 C is shown in Figure 6F. The Li–S cell with the OM-Mn_2O_3/S electrode showed the highest discharge capacities (851 mA h g^{-1} at 0.5 C, 740 mA h g^{-1} at 1.0 C, and 629 mA h g^{-1} at 2.0 C) at all the current densities, which were significantly higher than those of the Li–S cells with the other electrodes, owing to the reduced charge-transfer resistance of the OM-Mn_2O_3/S electrode.

26379368, 2024, 6, Downloaded from https://onlinelibrary.wiley.com/doi/10.1002/cey2.487 by Chung-Ang University, Wiley Online Library on [09/12/2024]. See the Terms and Conditions (https://onlinelibrary.wiley.com/terms-and-conditions) on Wiley Online Library for rules of use; OA articles are governed by the applicable Creative Commons License

An analysis of the extended cycling capabilities of Li–S cells constructed using the pristine sulfur, OM-Mn_2O_3/S, OM-Co_3O_4/S, and OM-NiO/S electrodes at a current density of 0.5 C is shown in Figure 6G. As expected, the Li–S cell with the OM-Mn_2O_3/S electrode showed the highest specific capacity, even after 250 cycles. It was confirmed that OM-TMOs can effectively anchor LPs during cell operation, and OM-Mn_2O_3 showed the best LP adsorption ability and enhanced conversion kinetics of the sulfur species. To evaluate the practical applicability of the electrodes, we conducted cycling tests under harsh conditions involving high sulfur mass loading of 6 mg_{sulfur} with a lean electrolyte condition of 8 $\mu L\ mg_{sulfur}^{-1}$ (Figure S7). On account of the increased sulfur loading, the active sulfur material in the pristine electrode was hardly utilized, owing to the increased thickness of the electrode and the lean electrolyte condition. In contrast, the OM-Mn_2O_3/S electrode delivered a high areal capacity of over 3.6 mA h cm^{-2}, which is much higher than that of commercial lithium-ion batteries (3 mA h cm^{-2}), because of the improved sulfur utilization originating from the accelerated sulfur redox reaction.[63]

As the shuttle reaction occurred, the migrated LPs were deposited on the Li metal surface and reduced to Li_2S/Li_2S_2. XPS analysis of the Li metal anode was conducted after 50 cycles to confirm that the shuttle effect was effectively suppressed. The XPS S 2p data obtained from the Li metal anode disassembled from the cycled Li–S cells with various electrodes are shown in Figure 7A–D. The lowest peak intensity of Li_2S and Li_2S_2 related to the LP deposits at 160.2 and 161.8 eV was observed on Li metal disassembled from the Li–S cell with an OM-Mn_2O_3/S electrode.[64,65] This result indicates that OM-Mn_2O_3 can effectively confine LPs during prolonged cycling compared with OM-Co_3O_4 and OM-NiO. In addition, owing to the high affinity between the LPs and OM-Mn_2O_3, the Li–S cell with the OM-Mn_2O_3/S electrode could operate even without $LiNO_3$, whereas the pristine electrode underwent an infinite charging state owing to the severe shuttle reaction (Figure S8). Furthermore, the smallest amount of LPs were dissolved in the open circuit voltage state owing to self-discharging, which was consistent with the XPS data (Figure S9). Overall, OM-Mn_2O_3 effectively anchored the LPs through chemical interactions and simultaneously protected the lithium metal anode by inhibiting the shuttle reaction during repeated cycling (Figure 8).

4 | CONCLUSIONS

Three TMOs with ordered mesoporous structures (OM-Mn_2O_3, OM-Co_3O_4, and OM-NiO) were prepared using mesoporous silica (KIT-6) as hard template to evaluate the efficiency of OM-TMOs as cathode host materials for LSBs. Among the three OM-TMOs, OM-Mn_2O_3 showed remarkable LP adsorption ability because of its strong interactions with LPs. In addition, it had the best catalytic ability for the reduction/oxidation conversion of LPs. Owing to the unique characteristics of OM-Mn_2O_3, LSBs with electrodes fabricated using the OM-Mn_2O_3/S composite delivered a high initial discharge capacity of 998 mA h g^{-1} at 0.5 C and maintained a discharge capacity of 561 mA h g^{-1} after 250 cycles. These values were significantly higher than those of the Li–S cell with a pristine sulfur electrode (initial discharge capacity of 671 mA h g^{-1} at 0.5 C and discharge capacity of 394 mA h g^{-1} after 250 cycles). Postmortem XPS analysis indicated that the superior cycling durability and reversibility of the OM-Mn_2O_3/S composite electrode were due to the alleviation of the LP shuttle effect during prolonged cycling. This study offers valuable guidance for the systematic design of the morphologies and compositions of cathode host materials for developing LSBs with improved electrochemical performance.

ACKNOWLEDGMENTS

Sung Joon Park, Yun Jeong Choi, and Hyun-seung Kim contributed equally to this study. This work was supported by a grant from the Korea Evaluation Institute of Industrial Technology (KEIT) funded by the Ministry of Trade, Industry & Energy (MOTIE) (No. 20012341). The authors gratefully acknowledge the support provided by the Technology Innovation Program (20010095, 20011173) funded by the Ministry of Trade, Industry, and Energy (MOTIE, Korea).

CONFLICT OF INTEREST STATEMENT

The authors declare that there are no conflicts of interests.

ORCID

Janghyuk Moon http://orcid.org/0000-0002-8965-1971
Young-Jun Kim http://orcid.org/0000-0002-9801-3066
Junyoung Mun http://orcid.org/0000-0001-9965-5709
Ki Jae Kim http://orcid.org/0000-0002-2166-7467

REFERENCES

1. Choi JW, Aurbach D. Promise and reality of post-lithium-ion batteries with high energy densities. *Nat Rev Mater*. 2016; 1(4):16013.
2. Armand M, Tarascon JM. Building better batteries. *Nature*. 2008;451(7179):652-657.
3. Qiao Y, Deng H, He P, Zhou H. A 500 Wh/kg lithium-metal cell based on anionic redox. *Joule*. 2020;4(7):1445-1458.
4. Manthiram A. Materials challenges and opportunities of lithium ion batteries. *J Phys Chem Lett*. 2011;2(3):176-184.
5. Goodenough JB, Park KS. The Li-ion rechargeable battery: a perspective. *J Am Chem Soc*. 2013;135(4):1167-1176.

26379368, 2024, 6, Downloaded from https://onlinelibrary.wiley.com/doi/10.1002/cey2.487 by Chung-Ang University, Wiley Online Library on [09/12/2024]. See the Terms and Conditions (https://onlinelibrary.wiley.com/terms-and-conditions) on Wiley Online Library for rules of use; OA articles are governed by the applicable Creative Commons License

6. Kim JH. Grand challenges and opportunities in batteries and electrochemistry. *Front Batter Electrochem*. 2022;1:1066276.
7. Yim T, Han SH, Park NH, et al. Effective polysulfide rejection by dipole-aligned $BaTiO_3$ coated separator in lithium–sulfur batteries. *Adv Funct Mater*. 2016;26(43):7817-7823.
8. Bhargav A, He J, Gupta A, Manthiram A. Lithium–sulfur batteries: attaining the critical metrics. *Joule*. 2020;4(2):285-291.
9. Manthiram A, Chung SH, Zu C. Lithium–sulfur batteries: progress and prospects. *Adv Mater*. 2015;27(12):1980-2006.
10. Zhou G, Chen H, Cui Y. Formulating energy density for designing practical lithium–sulfur batteries. *Nat Energy*. 2022;7(4):312-319.
11. Gao N, Li B, Zhang Y, et al. CoFe alloy-decorated interlayer with a synergistic catalytic effect improves the electrochemical kinetics of polysulfide conversion. *ACS Appl Mater Interfaces*. 2021;13(48):57193-57203.
12. Seh ZW, Sun Y, Zhang Q, Cui Y. Designing high-energy lithium–sulfur batteries. *Chem Soc Rev*. 2016;45(20):5605-5634.
13. Xiao M, Xing Z. Recent progress of lithium-sulfur batteries. *Batteries*. (2023;9(2):79.
14. Manthiram A, Fu Y, Chung SH, Zu C, Su YS. Rechargeable lithium–sulfur batteries. *Chem Rev*. 2014;114(23):11751-11787.
15. Kou Y, Jia J, Mi B, Yuan G, Wang Z. Rational design of 3DOM porous TiO_2 matrix decorated with Co nanoparticles as novel sulfur hosts for high-performance lithium-sulfur batteries. *Mater Lett*. 2022;327:133008.
16. Cui G, Li G, Luo D, et al. Three-dimensionally ordered macro-microporous metal organic frameworks with strong sulfur immobilization and catalyzation for high-performance lithium-sulfur batteries. *Nano Energy*. 2020;72:104685.
17. Zhang W, Xu Y, Liu J, et al. Waxberry-shaped ordered mesoporous P-TiO_{2-x} microspheres as high-performance cathodes for lithium–sulfur batteries. *Small Sci*. 2023;3(1):2200032.
18. Pan H, Cheng Z, Zhou Z, et al. Boosting lean electrolyte lithium–sulfur battery performance with transition metals: a comprehensive review. *Nano-Micro Lett*. 2023;15(1):165.
19. Cheng Z, Pan H, Wu Z, Wübbenhorst M, Zhang Z. Cu–Mo bimetal modulated multifunctional carbon nanofibers promoting the polysulfides conversion for high-sulfur-loading lithium–sulfur batteries. *ACS Appl Mater Interfaces*. 2022;14(40):45688-45696.
20. Cheng Z, Chen Y, Yang Y, et al. Metallic MoS_2 nanoflowers decorated graphene nanosheet catalytically boosts the volumetric capacity and cycle life of lithium–sulfur batteries. *Adv Energy Mater*. 2021;11(12):2003718.
21. Cheng Z, Wu Z, Chen J, et al. Mo_2N–ZrO_2 heterostructure engineering in freestanding carbon nanofibers for upgrading cycling stability and energy efficiency of Li–CO_2 batteries. *Small*. 2023;19(28):2301685.
22. Cheng Z, Lian J, Chen Y, et al. Robust in-Zr metal–organic framework nanosheets as ultrathin interlayer toward high-rate and long-cycle lithium–sulfur batteries. *CCS Chem*. 2023;1-11.
23. Cheng Z, Pan H, Chen J, Meng X, Wang R. Separator modified by cobalt-embedded carbon nanosheets enabling chemisorption and catalytic effects of polysulfides for high-energy-density lithium–sulfur batteries. *Adv Energy Mater*. 2019;9(32):1901609.
24. Manthiram A, Fu Y, Su YS. Challenges and prospects of lithium–sulfur batteries. *Acc Chem Res*. 2013;46(5):1125-1134.
25. Deng C, Wang Z, Wang S, Yu J. Inhibition of polysulfide diffusion in lithium–sulfur batteries: mechanism and improvement strategies. *J Mater Chem A*. 2019;7(20):12381-12413.
26. Hofmann AF, Fronczek DN, Bessler WG. Mechanistic modeling of polysulfide shuttle and capacity loss in lithium–sulfur batteries. *J Power Sources*. 2014;259:300-310.
27. Qie L, Zu C, Manthiram A. A high energy lithium–sulfur battery with ultrahigh-loading lithium polysulfide cathode and its failure mechanism. *Adv Energy Mater*. 2016;6(7):1502459.
28. Li Z, Zhang J, Guan B, Wang D, Liu LM, Lou XW. A sulfur host based on titanium monoxide@carbon hollow spheres for advanced lithium–sulfur batteries. *Nat Commun*. 2016;7:13065.
29. Zheng M, Chi Y, Hu Q, et al. Carbon nanotube-based materials for lithium–sulfur batteries. *J Mater Chem A*. 2019;7(29):17204-17241.
30. Liu X, Xiao Z, Lai C, et al. Three-dimensional carbon framework as high-proportion sulfur host for high-performance lithium–sulfur batteries. *J Mater Sci Technol*. 2020;48:84-91.
31. Ren J, Xia L, Zhou Y, Zheng Q, Liao J, Lin D. A reduced graphene oxide/nitrogen, phosphorus doped porous carbon hybrid framework as sulfur host for high performance lithium-sulfur batteries. *Carbon*. 2018;140:30-40.
32. Zhang Y, Sun K, Liang Z, Wang Y, Ling L. N-doped yolk-shell hollow carbon sphere wrapped with graphene as sulfur host for high-performance lithium–sulfur batteries. *Appl Surf Sci*. 2018;427:823-829.
33. Xiao Q, Li G, Li M, et al. Biomass-derived nitrogen-doped hierarchical porous carbon as efficient sulfur host for lithium–sulfur batteries. *J Energy Chem*. 2020;44:61-67.
34. Wang M, Xia X, Zhong Y, et al. Porous carbon hosts for lithium–sulfur batteries. *Chem Eur J*. 2019;25(15):3710-3725.
35. Liu YT, Liu S, Li GR, Yan TY, Gao XP. High volumetric energy density sulfur cathode with heavy and catalytic metal oxide host for lithium–sulfur battery. *Adv Sci*. 2020;7(12):1903693.
36. Liang X, Kwok CY, Lodi-Marzano F, et al. Tuning transition metal oxide–sulfur interactions for long life lithium sulfur batteries: the "Goldilocks". *Adv Energy Mater*. 2016;6(6):1501636.
37. Liu X, Huang JQ, Zhang Q, Mai L. Nanostructured metal oxides and sulfides for lithium–sulfur batteries. *Adv Mater*. 2017;29(20):1601759.
38. Wang H, Zhang W, Xu J, Guo Z. Advances in polar materials for lithium–sulfur batteries. *Adv Funct Mater*. 2018;28(38):1707520.
39. Ma F, Liang J, Wang T, et al. Efficient entrapment and catalytic conversion of lithium polysulfides on hollow metal oxide submicro-spheres as lithium–sulfur battery cathodes. *Nanoscale*. 2018;10(12):5634-5641.
40. Ding B, Shen L, Xu G, Nie P, Zhang X. Encapsulating sulfur into mesoporous TiO_2 host as a high performance cathode for lithium–sulfur battery. *Electrochim Acta*. 2013;107:78-84.
41. Dang R, Ma X, Liu J, Chen M, Zhang Y, Luo J. MnO_2/rGO/CNTs framework as a sulfur host for high-performance Li-S batteries. *Int J Hydrogen Energy*. 2018;25(8):1989.

26379368, 2024, 6, Downloaded from https://onlinelibrary.wiley.com/doi/10.1002/cey2.487 by Chung-Ang University, Wiley Online Library on [09/12/2024]. See the Terms and Conditions (https://onlinelibrary.wiley.com/terms-and-conditions) on Wiley Online Library for rules of use; OA articles are governed by the applicable Creative Commons License

42. Zhu Y, Wang S, Miao Z, Liu Y, Chou SL. Novel non-carbon sulfur hosts based on strong chemisorption for lithium–sulfur batteries. *Small*. 2018;14(40):1801987.
43. Choi DH, Ryoo R. Template synthesis of ordered mesoporous organic polymeric materials using hydrophobic silylated KIT-6 mesoporous silica. *J Mater Chem*. 2010;20(26):5544-5550.
44. Qian X, Jin L, Zhao D, et al. Ketjen black-MnO composite coated separator for high performance rechargeable lithium-sulfur battery. *Electrochim Acta*. 2016;192:346-356.
45. Li Y, Zhu J, Shi R, et al. Ultrafine and polar ZrO_2-inlaid porous nitrogen-doped carbon nanofiber as efficient polysulfide absorbent for high-performance lithium-sulfur batteries with long lifespan. *Chem Eng J*. 2018;349:376-387.
46. Pudukudy M, Yaakob Z. Sol-gel synthesis, characterisation, and photocatalytic activity of porous spinel Co_3O_4 nanosheets. *Chem Pap*. 2014;68(8):1087-1096.
47. Yan X, Tong X, Wang J, Gong C, Zhang M, Liang L. Rational synthesis of hierarchically porous NiO hollow spheres and their supercapacitor application. *Mater Lett*. 2013;95:1-4.
48. Svidrytski A, Hlushkou D, Thommes M, Monson PA, Tallarek U. Modeling the impact of mesoporous silica microstructures on the adsorption hysteresis loop. *J Phys Chem C*. 2020;124(39):21646-21655.
49. Häcker J, Nguyen DH, Rommel T, Zhao-karger Z, Wagner N, Friedrich KA. Operando UV/vis spectroscopy providing insights into the sulfur and polysulfide dissolution in magnesium–sulfur batteries. *ACS Energy Lett*. 2022;7(1):1-9.
50. Liang X, Hart C, Pang Q, Garsuch A, Weiss T, Nazar LF. A highly efficient polysulfide mediator for lithium–sulfur batteries. *Nat Commun*. 2015;6:5682.
51. Ren Y, Bhargav A, Shin W, Sul H, Manthiram A. Anode-free lithium–sulfur cells enabled by rationally tuning lithium polysulfide molecules. *Angew Chem*. 2022;134(55):e202207907.
52. Zhao M, Li BQ, Chen X, Xie J, Yuan H, Huang JQ. Redox comediation with organopolysulfides in working lithium-sulfur batteries. *Chem*. 2020;6(12):3297-3311.
53. Wen G, Sui Y, Zhang X, et al. Mn_3O_4 anchored polypyrrole nanotubes as an efficient sulfur host for high performance lithium–sulfur batteries. *J Colloid Interface Sci*. 2021;589:208-216.
54. Li S, Fan Z. Encapsulation methods of sulfur particles for lithium–sulfur batteries: a review. *Energy Storage Mater*. 2021; 34:107-127.
55. Shankar S, Pangeni R, Park JW, Rhim JW. Preparation of sulfur nanoparticles and their antibacterial activity and cytotoxic effect. *Mater Sci Eng C*. 2018;92:508-517.
56. Liu X, Qian T, Liu J, Tian J, Zhang L, Yan C. Greatly improved conductivity of double-chain polymer network binder for high sulfur loading lithium–sulfur batteries with a low electrolyte/sulfur ratio. *Small*. 2018;14(33):1801536.
57. Huang X, Wang Z, Knibbe R, et al. Cyclic voltammetry in lithium–sulfur batteries—challenges and opportunities. *Energy Technol*. 2019;7(8):1801001.
58. Wild M, O'Neill L, Zhang T, et al. Lithium sulfur batteries, a mechanistic review. *Energy Environ Sci*. 2015;8(12):3477-3494.
59. Song JK, Kim M, Park S, Kim YJ. LiTFSI salt concentration effect to digest lithium polysulfides for high-loading sulfur electrodes. *J Energy Chem*. 2023;78:574-581.
60. Park SJ, Yang SY, Han SA, et al. Two-in-one separator capturing and reutilizing polysulfides for high performance lithium–sulfur batteries. *Chem Eng J*. 2023;460:141620.
61. Zerrin T, Shang R, Dong B, et al. An overlooked parameter in Li–S batteries: the impact of electrolyte-to-sulfur ratio on capacity fading. *Nano Energy*. 2022;104:107913.
62. Chen Y, Wu J, Li Y. A "catalysis-immobilization-deposition" stepwise strategy toward dynamic equilibrium of polysulfides conversion and diffusion in lithium–sulfur batteries. *Small Methods*. 2023;7(7):2300086.
63. Duffner F, Kronemeyer N, Tübke J, Leker J, Winter M, Schmuch R. Post-lithium-ion battery cell production and its compatibility with lithium-ion cell production infrastructure. *Nat Energy*. 2021;6(2):123-134.
64. Zha C, Wang S, Liu C, et al. Single-atom tailoring of Li_2S to form Li_2S_2 for building better lithium–sulfur batteries. *Energy Stor Mater*. 2022;47:79-86.
65. Wu, Y, Momma, T, Ahn, S, Yokoshima, T, Nara, H, Osaka, T On-site chemical pre-lithiation of S cathode at room temperature on a 3D nano-structured current collector. *J Power Sources* 2017;366:65-71.

SUPPORTING INFORMATION

Additional supporting information can be found online in the Supporting Information section at the end of this article.

How to cite this article: Park SJ, Choi YJ, Kim H-S, et al. Stable immobilization of lithium polysulfides using three-dimensional ordered mesoporous Mn_2O_3 as the host material in lithium–sulfur batteries. *Carbon Energy*. 2024;6:e487. doi:10.1002/cey2.487

26379368, 2024, 6, Downloaded from https://onlinelibrary.wiley.com/doi/10.1002/cey2.487 by Chung-Ang University, Wiley Online Library on [09/12/2024]. See the Terms and Conditions (https://onlinelibrary.wiley.com/terms-and-conditions) on Wiley Online Library for rules of use; OA articles are governed by the applicable Creative Commons License